Eur. Phys. J. Plus (2021) 136:829
https://doi.org/10.1140/epjp/s13360-021-01780-7

THE EUROPEAN PHYSICAL JOURNAL PLUS

Regular Article

Investigation of Cr substitution effect on the evolution of $La_{0.67}Ca_{0.2}Ba_{0.13}Fe_{1-x}Cr_xO_3$ ($x = 0$ and 0.03) electrical properties under frequency and temperature variation

Ah. Dhahri[2,3,a], Amira Bougoffa[1,b], A. Zaouali[1], A. Benali[1,3,4], M. P. F. Graça[4], M. A. Valente[4], B. F. O. Costa[3], N. Abdelmoula[2], José F. M. L. Mariano[5]

[1] Laboratoire de Physique Appliquée, Faculté des Sciences, Université de Sfax, 3000 Sfax, Tunisia
[2] Laboratoire des Matériaux Multifonctionnels et Applications, Faculté des Sciences, Université de Sfax, 3000 Sfax, Tunisia
[3] CFisUC, Physics Department, University of Coimbra, 3004-516 Coimbra, Portugal
[4] I3N, Physics Department, University of Aveiro, Campus de Santiago, Aveiro, Portugal
[5] Department of Physics and CeFEMA, Faculty of Science and Technology, University of Algarve, Campus de Gambelas, 8005-139 Faro, Portugal

Received: 8 April 2021 / Accepted: 20 July 2021

Abstract In this study, $La_{0.67}Ca_{0.2}Ba_{0.13}Fe_{1-x}Cr_xO_3$ ($x = 0$ and 0.03) powders were prepared by auto-combustion method. The examination of the purity and crystalline structure of the samples by X-ray diffraction showed a cubic structure formed with the $Pm\bar{3}m$ space group. Scanning electron microscopy was used to study the morphology and grains size, indicating an agglomeration of nanometric particles. Impedance spectroscopy in the temperature range from 200 to 360 K was used in order to understand the evolution of the electrical behavior of the substituted perovskites. The real and imaginary parts of the impedance were adjusted with two different equivalent circuits. The activation energies extracted from the imaginary part of the impedance, and the electrical conductivity was very closed indicating a transformation of the electrical behavior. This was confirmed by a decrease in the resistance after substitution of Fe cations by Cr ones. AC conductivity studies showed a Jonscher's behavior and a change of conduction process from a succession of NSPT and CBH model to the existence of only CBH one after the substitution.

1 Introduction

Perovskite structured materials belong to a large family of oxides that appeared as multifunctional materials in the last years [1–7]. Different research works mention a large modification in their optical, electrical and magnetic properties [8–11] which can be the result of several factors [12–17]. In this kind of materials, a small substitution of the constituting cations induces a mixed valence due to the different oxidation states of the new

[a] e-mail: ahmed.dhahri@live.fr (corresponding author)
[b] e-mail: amirabougoffa@gmail.com

Published online: 11 August 2021

introduced cations [18], resulting in the modification of the physical properties and enhancing their application fields. As reported by Yue et al. [19], the substitution of La by Sr in $LaMnO_3$ material leads the reduction of the gap energy. Another study of Polat et al. proved a decrease in the activation energy and the AC conductivity after substitution of Y cations by Os ones in $YMnO_3$ perovskite structured material [20]. By linking impedance and conductivity measurements, the evolution of the electrical properties of the substituted perovskite materials can be explained by the increase in the density of charge carriers and the decrease in the cations separation distance after the substitution process [21]. These properties enhance their use in several electronic devices such as solar cells, diode capacitor. [22–24].

Due to the increase in energy consumption and the depletion of conventional resources, it is necessary to search for new efficient materials at a low cost and with a simple synthesis process. Ferrites have attracted the attention of scientific researchers because of their low cost and their applications in several fields, such as chemical sensors, fuel cells, lithium batteries, supercapacitors [25] and magnetic materials [4, 26]. Several studies have been carried out to understand the correlation between the different physical properties (structural, catalytic, magnetic, dielectric…) Following partial substitution in site A; $La_{1-x}AFeO_3$ (A = Sr, Ba, Ca, Pb…) [27] or in the site B, $LaFe_{1-x}B_xO_3$ (B = Co, Mg, Mn….) [28, 29] of the parent compound $LaFeO_3$.

The interest in these materials for basic science and industrial use has directed researchers to modify the properties of these materials to understand experimental observations and the resulting physics. The properties of ferrites can be adjusted for specific purposes by appropriate substitutions of bivalent and trivalent rare earth and alkaline earth elements at site A and other transition metals at site B [30, 31]. The interest of the substitution of Fe by Cr in ferrites lies in the fact that Cr ions can exist in the structure with different valence, spin-orbital states, and the expected wide variety of magnetic and electrical phenomena associated with different levels of substitution. Cr^{3+} ions ($3d^3$) have an ionic radius significantly smaller than that of Fe^{3+} ($r_{Cr3+} = 0.615$ Å; $r_{Fe3+} = 0.645$ Å). The effect of Cr doping on the structural and dielectric properties of ferrites is of considerable practical and scientific interest [32]. To determine the magnetic and magneto-transport behavior in doped ferrites, it is necessary to study, in addition to the effects of substitution at the B (Fe) site, other factors such as the mean radius $\langle r_A \rangle$ of the ions at site A, the size mismatch between these ions and lattice distortion [33, 34]. In this context, different scenarios have been proposed to modify the conduction mechanism including the substitution of La by a mixture of cations (such as Ba and Sr). This latter scenario, however, resulted in a significant decrease in the strength of the $La_{0.67}Ca_{0.2}Ba_{0.13}Fe_{1-x}Cr_xO_3$ mixture [34].

On another hand, several published studies mention that the synthesis method can strongly affect the structure, the morphology and the physical properties of these materials [35]. There are several techniques reported in the literature to prepare perovskite materials; among them, we can note: co-precipitation [36], hydrothermal [37] sol–gel [38] and auto-combustion [39]. This later presents the most famous process that links an easy processing and pure obtained materials.

Therefore, the aim of this study is to investigate the effect of substituting Fe ions by Cr ones in $La_{0.67}Ca_{0.2}Ba_{0.13}Fe_{1-x}Cr_xO_3$ prepared by auto-combustion synthesis method. The X-ray diffraction (XRD), the EDS and the scanning electronic microscopy (SEM) were used to evaluate the structure, the microstructure and the purity of the prepared samples. The impedance spectroscopy measurements were recorded to study the evolu-

tion of the electrical and dielectric properties as a function of frequency and temperature.

2 Experimental

2.1 Samples preparation

The auto-combustion method used to prepare the samples is described as follows: sol–gel preparation of $La_{0.67}Ca_{0.2}Ba_{0.13}Fe_{1-x}Cr_xO_3$ powders was started by dissolving stoichiometric amounts of nitrates precursors ($La(NO_3)_3{\cdot}6H_2O$; calcium nitrate $Ca(NO_3)_2$; $Ba(NO_3)_2$; $Fe(NO_3)_3{\cdot}9H_2O$ and $Cr(NO_3)_3$ in distilled water. After that, glycine ($C_2H_5NO_2$) was added to the solution as a fuel agent in the ratio: $G/M = 1.2$ to the metal ions. When temperature raised to 80 °C, a viscous gel was obtained that was annealed at 180 °C. Then, temperature was raised to 300 °C to ensure a self-combustion leading to the formation of a black powder. Finally, the obtained powder was pressed into pellets and sintered at 700 °C.

2.2 Measurements tools

The X-ray powder diffraction (XRD) of the prepared powders was recorded at room temperature using a D8 ADVANCE, Bruker Diffractometer with copper anticathode over the 5°–90° of Bragg angles range. Subsequently, powder morphology was examined by a TESCAN VEGA3 SBH scanning electron microscope (SEM) equipped with an EDS detector Bruker XFlagh 410 M for elemental composition and homogeneity check of the prepared samples.

For electrical measurements, the pellet was mechanically compressed between two parallel platinum plates functioning as electrodes. Then, transport properties of the perovskites were measured using a Network Analyzer Agilent 4294 in the frequency range 100 Hz–1 MHz and the temperature range 260–360 K.

3 Results and discussion

3.1 Crystalline structure and morphology

The XRD patterns recorded at room temperature are displayed in Fig. 1a, b. The Fullprof software was used to examine the phase purity and the crystalline structure of the prepared materials [40]. The refinement results, illustrated in Table 1, proved a cubic structure with the $Pm\bar{3}m$ space group for both compounds with cell parameters of 3.9063 Å and 3.9042 Å, respectively, for $x = 0$ and $x = 0.03$, respectively. The observed small decrease in the lattice parameters values after the substitution process can be related to the small ionic radii of Cr ions [41].

To estimate the average size of crystallites, we have recorded to the Williamson–Hall equation given by the following relation [42]:

$$\beta \cos\theta = \frac{k\lambda}{D_{\text{W-H}}} + \varepsilon 4 \sin\theta \tag{1}$$

where $K = 0.9$ is the form factor, $\lambda = 1.5406$ Å is the used wavelength, θ is the diffraction angle of the most intense peak, and β is the width at half maximum of the most intense peak.

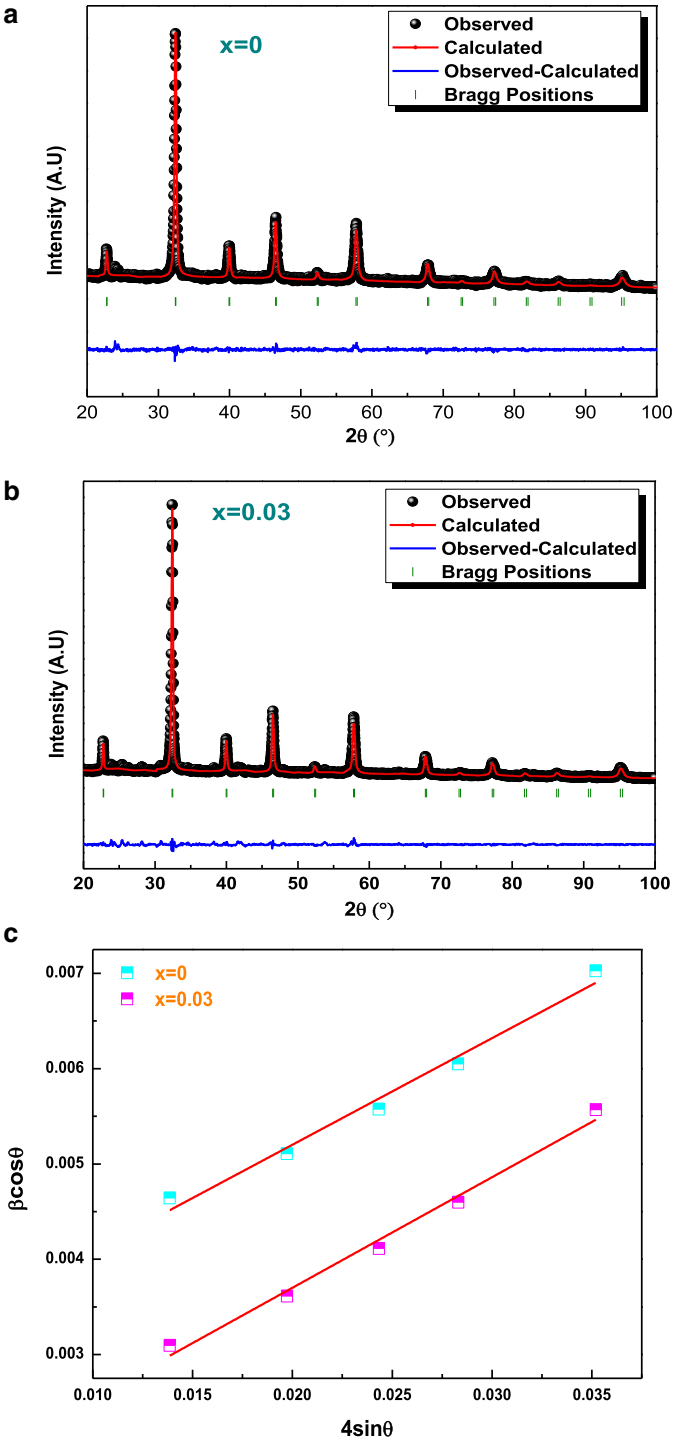

Fig. 1 **a** The refined XRD patterns of $x = 0$ sample, **b** the refined XRD patterns of $x = 0.03$ sample and **c** the plots $\beta \cos\theta$ versus $4 \sin\theta$ of both $x = 0$ and $x = 0.03$ samples

Table 1 Extracted parameters from the Rietveld refinement and SEM observation for both $x = 0.0$ and $x = 0.03$ compounds

	$x = 0$	$x = 0.03$
a (A)	3.906_3	3.904_2
D_{XRD} (nm)	38.36_5	27.14_4
$D_{W\text{-}H}$ (nm)	100.47_3	46.84_2
Strain	0.11_1	0.11_1
D_{SEM} (nm)	755	703

Then, the strain ε was obtained from the slope of the curve $\beta \cos\theta$ versus 4. $\sin\theta$, as shown in Fig. 1c. After that, the size of the crystallites $D_{W\text{-}H}$ was estimated from the interception of the linear fit.

By considering the stress factor ε close to zero, Eq. (1) can be expressed differently to give the Debye Scherrer formula written as [43]:

$$D_{SC} = \frac{K \cdot \lambda}{\beta \cdot \cos\theta} \tag{2}$$

The calculated values of D_{sc} and $D_{W\text{-}H}$ are illustrated in Table 1. The observed decrease in the crystallites size can be due to the fact that the ionic radii of Cr^{3+} ($r_{Cr3+} = 0.615$ Å) cation are lower than the Fe^{3+} cation's one ($r_{Fe3+} = 0.645$ Å).

Figure 2a, b shows the EDS and SEM observations of $x = 0.0$ and $x = 0.03$ samples. We can clearly observe the uniform distribution of all elements throughout the perovskite powder as well as the presence of Cr element in $x = 0.03$ sample. The estimation of particle size from the SEM images employing the "ImageJ" software noted the presence of nanoparticles agglomeration with a decrease from approximately 755 nm for the sample $x = 0$ to 702 nm for $x = 0.03$ one, as demonstrated by the extracted histograms shown also in Fig. 2.

3.2 Complex impedance analysis

In this study, we have performed impedance spectroscopy measurements in order to investigate the effect of Cr substitution on the electrical properties of $La_{0.67}Ca_{0.2}Ba_{0.13}FeO_3$ material.

Figure 3a, b displays the evolution of the real (Z') versus frequency for $x = 0$ and $x = 0.03$ compounds.

The variation of Z' of $La_{0.67}Ca_{0.2}Ba_{0.13}Fe_{1-x}Cr_xO_3$ ($x = 0$ and 0.03) as a function of temperature and frequency presents three distinct behaviors for both samples. In the first region (1), corresponding to the low frequencies, the values of (Z') decrease progressively as the temperature increases independently of the frequency. The constant (Z') values of our samples at different temperatures pointing out to an accumulation of charge carriers at the grain boundaries [8]. The high mobility of charge carriers in the second region (2) causes a gradual decrease in the amplitude of Z' as the temperature and frequency increase, thus causing an increase in AC conductivity. The values of Z' merge independently of the temperature at high frequencies (3). This behavior could possibly be related to the release of the space charge. In fact, the charge barrier could gradually decrease under the influence of temperature [44, 45] thus causing a considerable reduction in the resistance of AC current to become negligible and hence, an improvement in conduction.

Generally, each electroactive region of polycrystalline materials is represented by a parallel resistance–capacitance (RC) element. In the imaginary impedance (Z'') plots, a Debye peak is associated with each RC component whose values of frequency f_{max} and amplitude Z''_{max}

are given by $2\pi f_{max} \cdot RC = 1$ and $Z''_{max} = R/2$, respectively. It can also be seen as a semicircle in the Z'' versus Z' plots whose the equivalent circuit of the sample will be formed by a series of these parallel RC elements. The values of R and C of the equivalent electrical circuit can be determined from those of Z''_{max} using the two preceding equations.

The variation of the imaginary part of the impedance (Z'') in function of the frequency of both compounds is plotted for different temperatures in Fig. 4a, b. It can be noted that all curves present a maximum value, $Z''_{max,}$ that decreases with increasing temperature indicating a

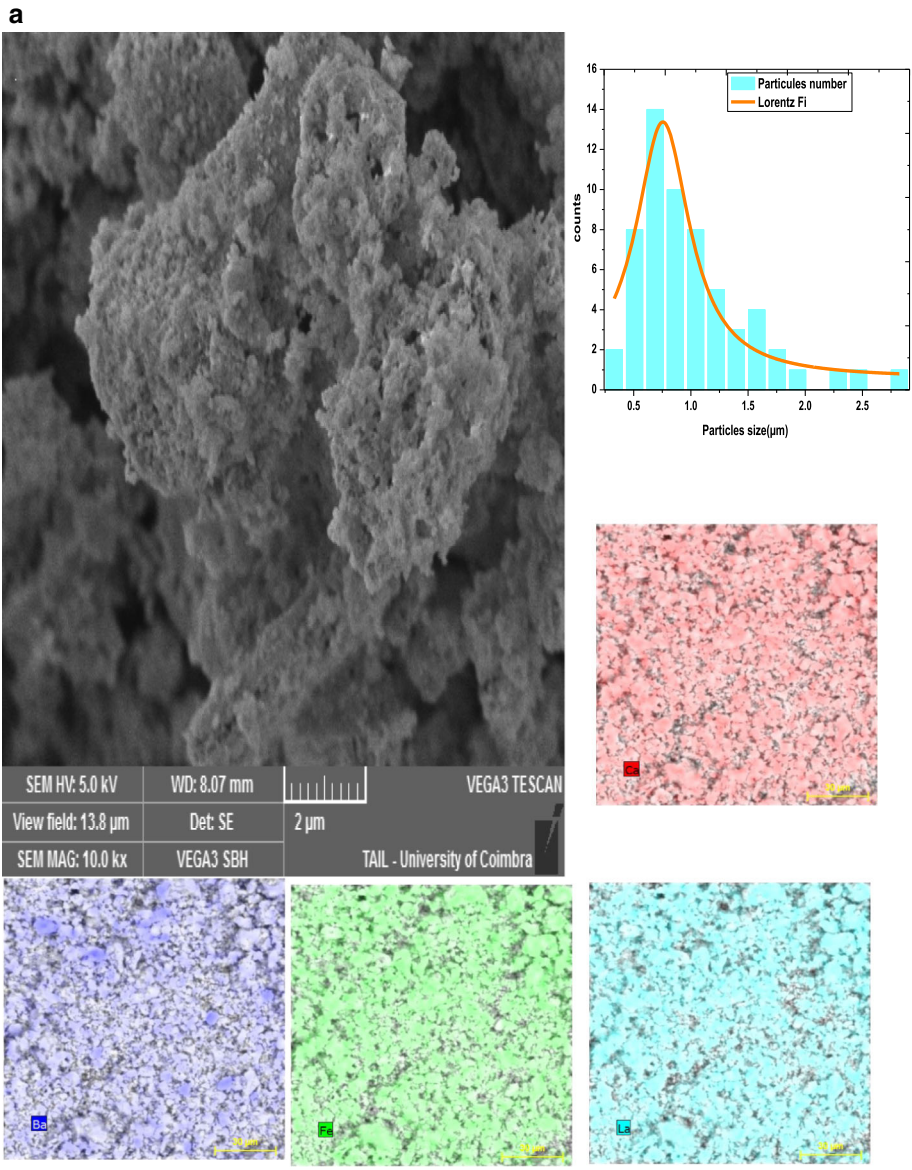

Fig. 2 The EDS and SEM images: **a** $x = 0$, **b** $x = 0.03$

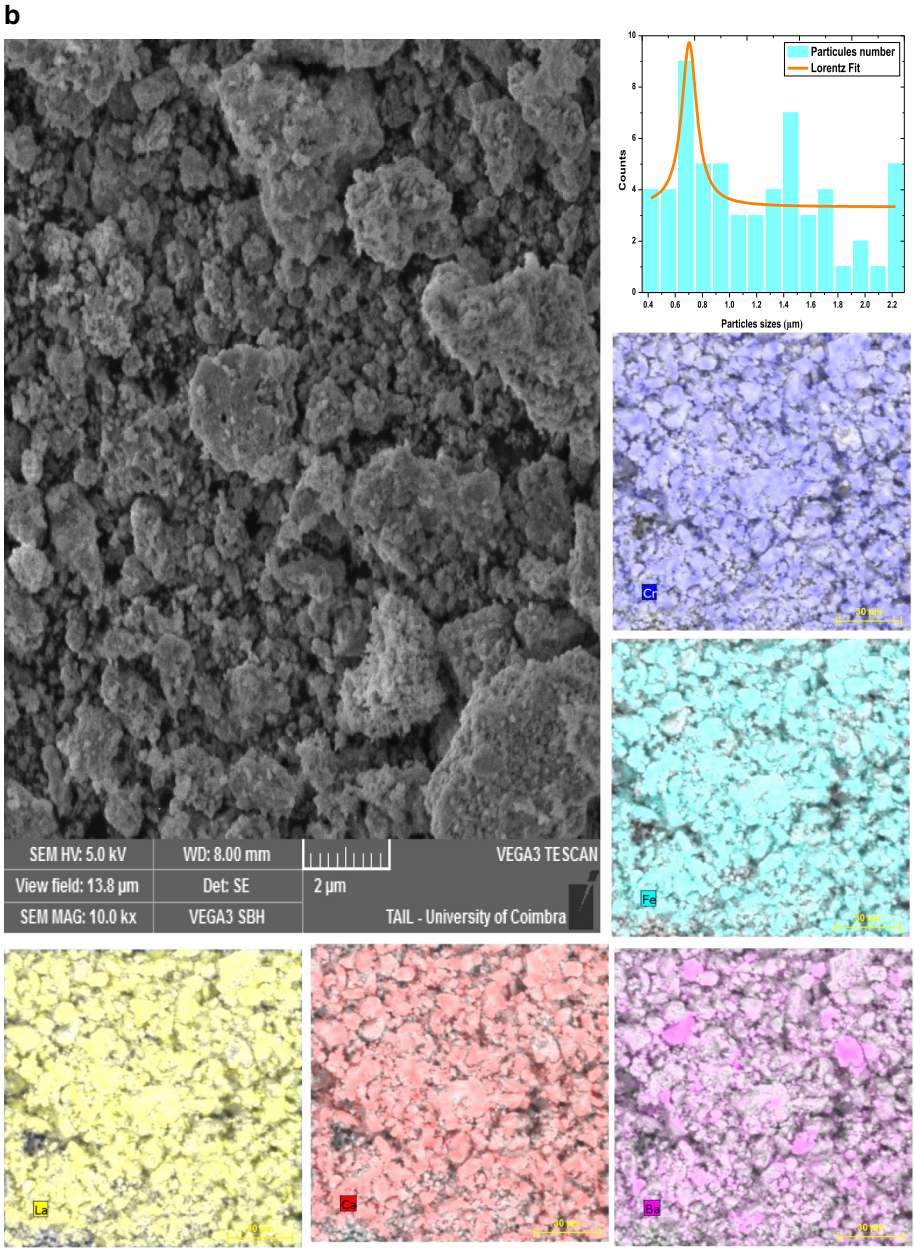

Fig. 2 continued

single relaxation peak at a characteristic frequency (f_{max}). The only dielectric relaxation was confirmed by adopting several considerations: (1) no modification of the slope in the relative representation of Z' with respect to Z''/f [shown in supplementary material, see Fig. S1 and Fig. S2] [46] and (2) a unique arc at each temperature in the impedance planes (Fig. 5). The relaxation frequencies of the grain and the grain boundaries are very close, thus inducing

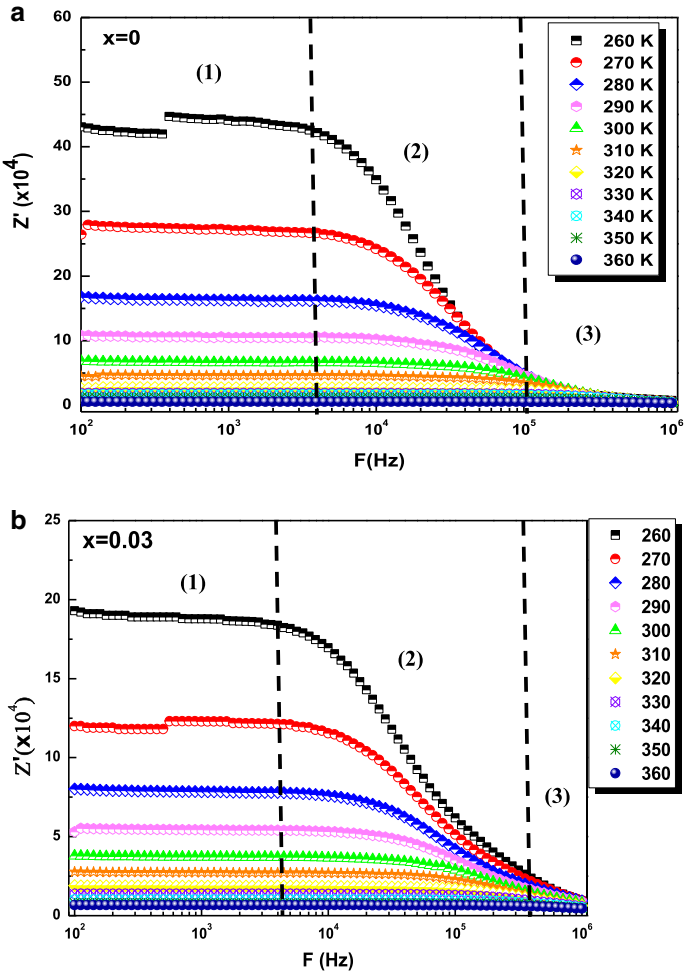

Fig. 3 The Real real part of the impedance plots as a function of frequency at different temperatures of: **a** $x = 0$, **b** $x = 0.03$

a unique relaxation in the Z'' spectra resulting from a high degree of overlap between the contributing elements.

We can clearly see that the relaxation peak shifts to the high frequency region, which can induce an increase in the relaxation time and a decrease in the resistance of the bulk material [47]. Accordingly, this result confirms the Arrhenius behavior in the studied compounds [48]. Moreover, at higher frequencies, we observe a merging in the Z'' plots that can be attributed to a space charge accumulation in the material because it does not require more time to relax due to the space charge polarization decreasing with the frequency rising [49].

It is important to mention that the substitution of Fe ions by Cr ones results in a shift of the relaxation peak to high frequencies with a decrease in the Z''. By adding this effect to the temperature effect, we can assume that the substitution process can enhance the electrical properties of the studied material. These results were confirmed by the decrease in the acti-

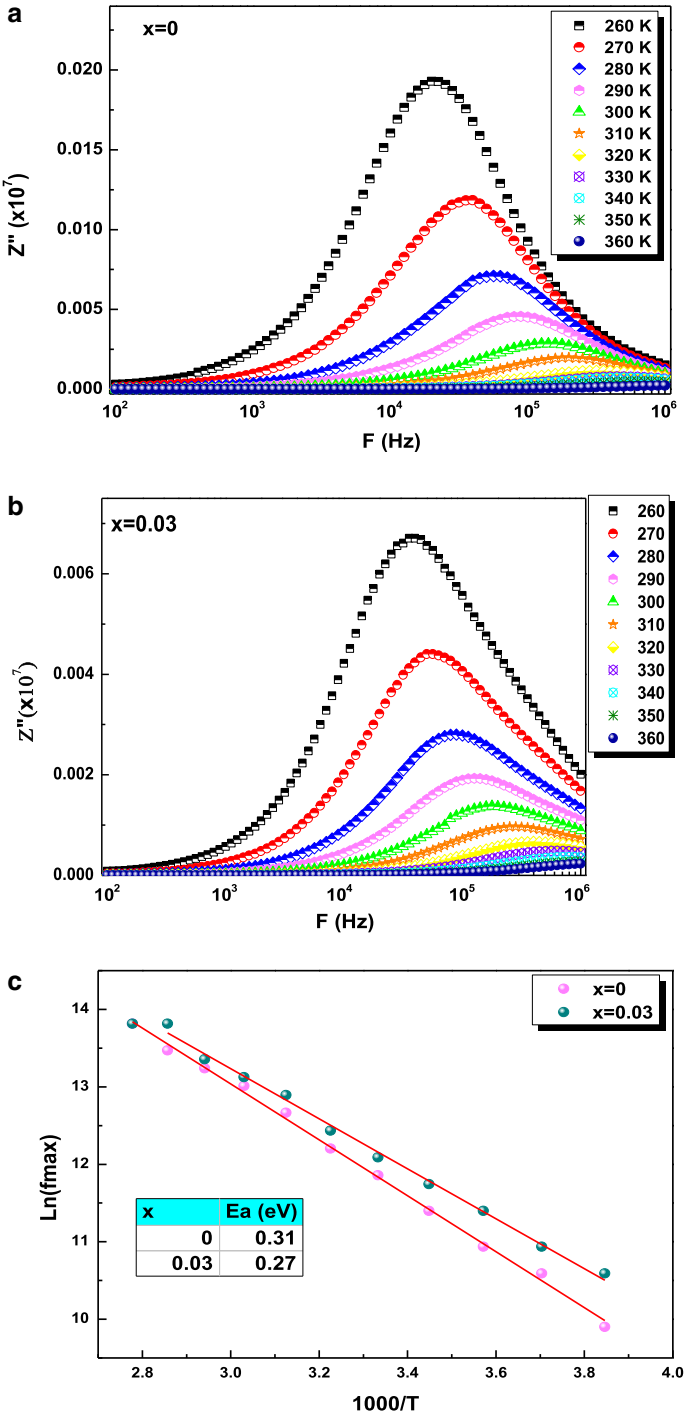

Fig. 4 The imaginary part of the impedance plots as a function of frequency at different temperatures of: **a** $x = 0$, **b** $x = 0.03$, **c** variation of $\mathrm{Ln}(f_{max})$ as a function of 1000/T of both $x = 0$ and $x = 0.03$ samples

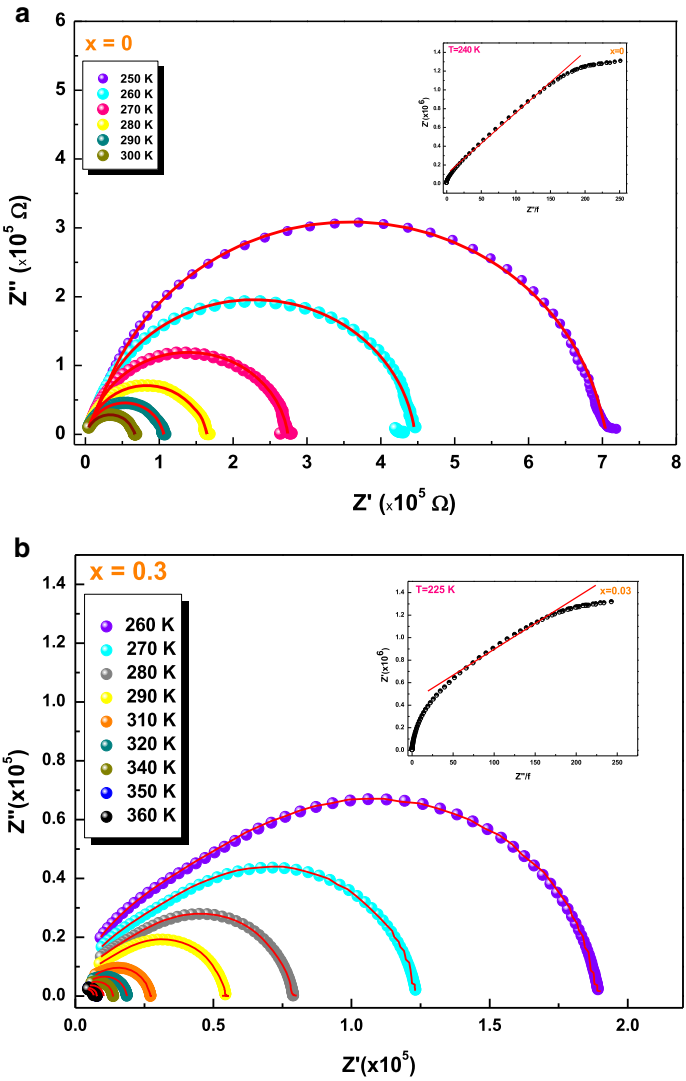

Fig. 5 The impedance Nyquist plots of: **a** $x = 0$, **b** $x = 0.03$

vation energy after substitution, as proved by the logarithmic variation of $\mathrm{Ln}(f_{\max})$ versus 1000/T displayed in Fig. 4c according to the following Arrhenius law [50]:

$$f_{\max} = f_0 \exp\left(-\frac{E_a}{K_B T}\right) \tag{3}$$

where $f_{\max}$ represents the frequency attributed to the maximum value of the imaginary part of the complex impedance Z'' for each temperature, f_0 is a pre-exponential factor, E_a is the activation energy, and k_B is the Boltzmann constant.

Figure 5a, b shows the Nyquist plots of both $x = 0$ and $x = 0.03$ compounds. As observed, all curves present the form of semicircles where the diameters decrease as the temperature

Table 2 Theoretical parameters obtained from the fitted data with the equivalent circuit for $x = 0$

(*a*)	Electrode contribution			Boundary grain contribution			Grain contribution		
T (K)	R ($\times 10^5$ Ω)	CPE ($\times 10^{-11}$ F)	α	R ($\times 10^4$ Ω)	CPE ($\times 10^{-11}$ F)	α	R ($\times 10^3$ Ω)	CPE ($\times 10^{-10}$ F)	α
250	9.184	3.444	0.948	4.478	4.536	0.584	6.820	1.302	0.947
260	4.338	3.727	0.947	2.237	6.877	0.736	4.298	1.998	1.048
270	2.689	3.959	0.931	1.344	8.562	1.277	3.432	2.783	1.118
280	1.488	4.335	0.922	0.874	10.122	0.459	2.428	4.300	1.911
290	0.838	4.747	0.910	0.677	21.063	0.707	1.667	3.988	0.947
300	0.498	5.020	0.898	0.376	33.23	0.479	1.185	4.563	1.111

Table 3 Theoretical parameters obtained from the fitted data with the equivalent circuit for $x = 0.03$

T (K)	Grain contribution			Grain boundary contribution	
	R ($\times 10^5$ Ω)	CPE ($\times 10^{-10}$ F)	α	R ($\times 10^4$ Ω)	CPE ($\times 10^{-11}$ F)
260	1.667	1.831	0.837	2.464	1.258
270	1.061	1.690	0.853	1.805	1.188
280	0.662	1.636	0.865	1.290	1.170
290	0.444	1.553	0.877	1.019	1.150
300	0.291	1.179	0.903	0.817	1.164
310	0.175	5.861	0.751	0.967	9.507
320	0.120	7.962	0.740	0.675	8.244
330	0.089	5.831	0.762	0.474	8.663
340	0.066	2.931	0.806	0.360	9.058
350	0.051	2.029	0.830	0.265	8.990
360	0.047	1.450	0.850	0.191	1.090

increases indicating a thermally activated conduction process [51]. The observed semicircle decentralization indicates a non-Debye-type relaxation process [52].

To put it differently, we have fitted the impedance experimental data to an equivalent circuit using the Z-view software. The fitting process leads to a series combination of Rg//CPEg, Rgb//CPEgb and Re//CPEe, for $x = 0$ material and a series combination of Rg//CPEg, Rgb//Cgb for $x = 0.03$ one. This difference can be due to the experimental process during the electrode deposition.

The theoretical parameters extracted from the equivalent circuits adjustment at different temperatures for $x = 0$ and $x = 0.03$ compounds are summarized, respectively, in Tables 2 and 3.

4 Electrical analysis

4.1 DC conductivity

The logarithmic variation of the ac conductivity versus 1000/T of the studied materials at different frequencies, displayed in Fig. 6a, b, proves a linear variation that changes the slope at low-temperature range. Accordingly, we can assume the presence of two different conduction mechanisms with dissimilar activation energies.

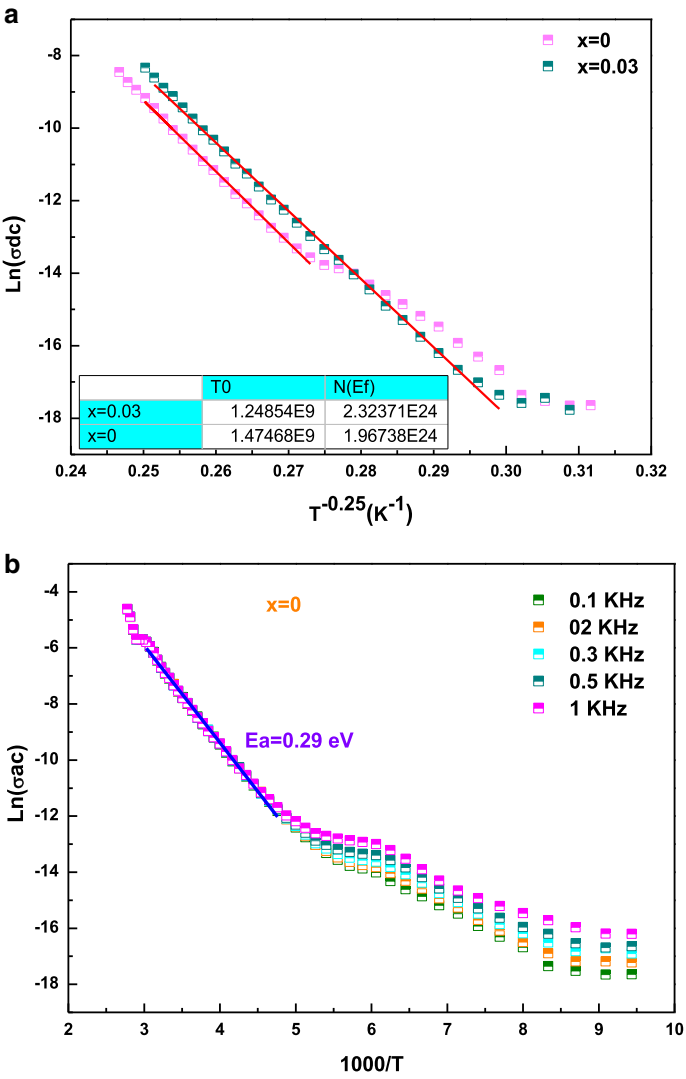

Fig. 6 **a** The variation of $\ln\sigma_{dc}$ versus $T^{-0.25}$ for both $x = 0.0$ and $x = 0.03$ compounds, **b** and **c** the logarithmic variation of the σ_{dc} versus 1000/T at high temperature region, **d** the variation of the activation energy versus temperature at low temperature region

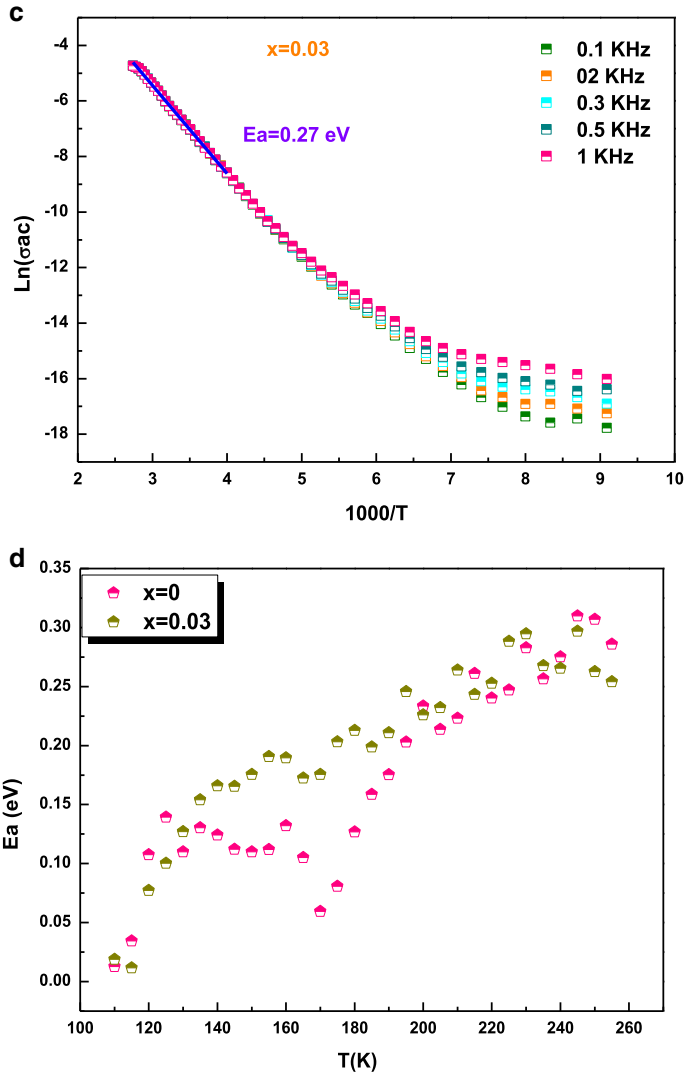

Fig. 6 continued

Therefore, at higher temperatures, it can be suggested that the charge hopping occurs only between the neighboring sites supposing then that the independence of the hopping range and the activation energy on temperature variation as assumed by the Arrhenius model given by the following equation [53]:

$$\sigma_{dc} = \sigma_0 \exp\left(-\frac{E_a}{k_B T}\right) \tag{4}$$

While at low temperatures, Mott supposed that the hopping range in this region can be larger than the distance between the neighboring equivalent sites because of the lower involved activation energy indicating a variable-range hopping (VRH) process [54]. This behavior was confirmed by a linear variation of $\mathrm{Ln}(\sigma_{dc})$ versus $T^{-0.25}$ as demonstrated by Fig. 6a. This

kind of behavior can be explained by the decrease in the free carrier's concentration at low temperatures and the low thermal energy unable to activate the hopping process as observed in several researches on perovskite materials [55–57]. In this case, the DC conductivity can be expressed as [54]:

$$\sigma_{dc} = \sigma_0 \exp\left(-\left(T_0/T\right)^{\frac{1}{4}}\right) \tag{5}$$

being σ_0 a constant and T_0 the Mott's characteristic temperature, given by the following expression:

$$T_0 = \frac{16}{k_B \cdot N(E_F) \cdot \alpha^3} \tag{6}$$

$N(E_F)$ represents the density of states near the Fermi energy, and α refers to the decay factor of the localized wave function.

The calculated values of $N(E_F)$ prove an increase after the substitution process which is in agreement with the variation of the activation energy of the grain as shown in Fig. 6b, c.

In this case, the effect of temperature on the evolution of the activation energy of the bulk conductivity, $E_{a,}$ is governed by the following expression [53]:

$$E_a = -\frac{d(\mathrm{Ln}(\sigma_{dc}))}{d\left((k_B T)^{-1}\right)} \tag{7}$$

Thus, the variation of E_a with temperature displayed in Fig. 6d is different from the above Arrhenius model that assumes its independence on temperature.

The dependence on temperature of hopping energy $W(T)$, displayed in Fig. 7a, b follows Eq. (8) given by [53]:

$$W = \frac{k_B \cdot T^{\frac{3}{4}} \cdot T_0^{\frac{1}{4}}}{4} \tag{8}$$

As clearly seen, the hopping energy W increases as temperature rises assuming a polaronic VRH conduction dynamics for both $x = 0$ and $x = 0.03$ samples.

In the same figures, we have displayed the variation mean hopping distance R_h(T) given by the following equation [53]:

$$R_h = \frac{3}{8} \cdot \alpha \cdot \left(\frac{T_0}{T}\right)^{\frac{1}{4}} \tag{9}$$

The thermal variation of R_h proves that the hopping distance decreases indicating 250 K as a maximum temperature corresponding to the shortest hopping distance and favoring the dominance of the VRH process [56]. This temperature presents also the crossover point from VRH to the Arrhenius.

4.2 AC conductivity analysis

The AC conductivity dependence on the frequency of both $x = 0$ and $x = 0.03$ samples was investigated under the temperature range 260–360 K.

Indeed, Fig. 8a, b proves that the ac conductivity spectra of the studied perovskite materials follow the Jonscher's power law expressed as [58]:

$$\sigma_{ac} = \sigma_{dc} + A\omega^s \tag{10}$$

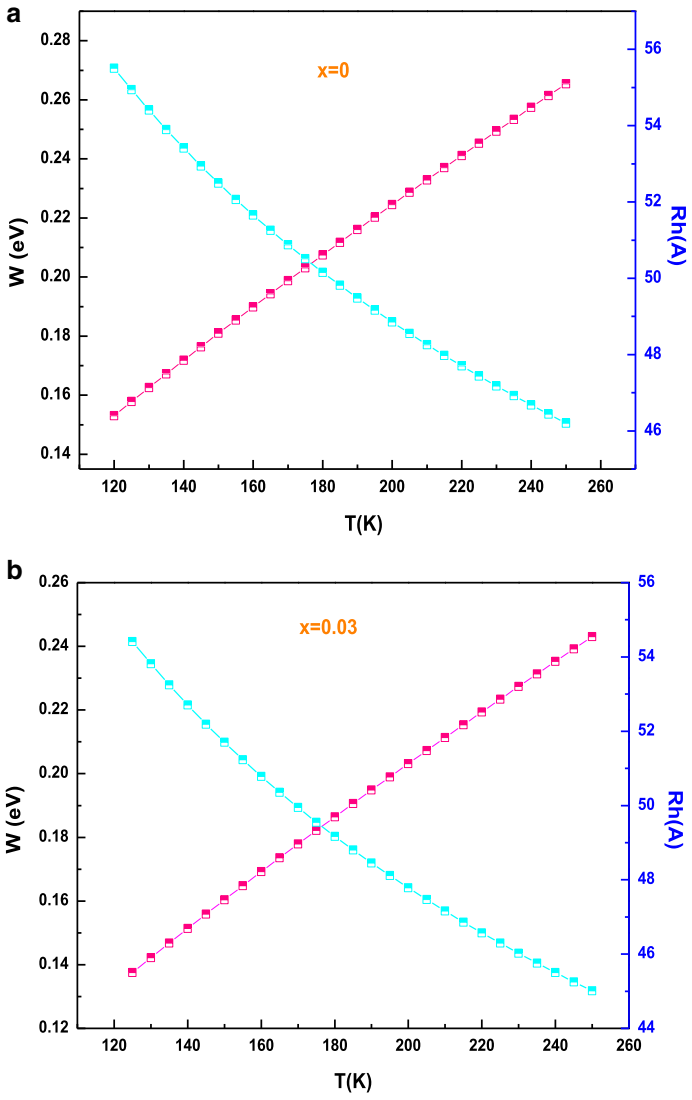

Fig. 7 The variation of the hopping energy and hopping distance versus temperature: **a** $x = 0$, **b** $x = 0.03$

where σ_{dc} represents the direct current conductivity, ω refers to the angular frequency, (s) is a parameter depending on temperature and presenting the degree of interaction between mobile ions and the lattices around them [59]. A represents a constant related to the strength of polarizability.

The experimental data of the $\sigma_{ac}(f)$ were adjusted according to Eq. (10) in order to identify the conduction process in the studied materials.

As observed in Fig. 8a, b, the AC conductivity spectrum of both samples remains almost constant at low frequencies (10^2–10^5 Hz). After that, they begin to increase, which can be attributed to the relaxation of the ionic atmosphere after the movement of the particles [60].

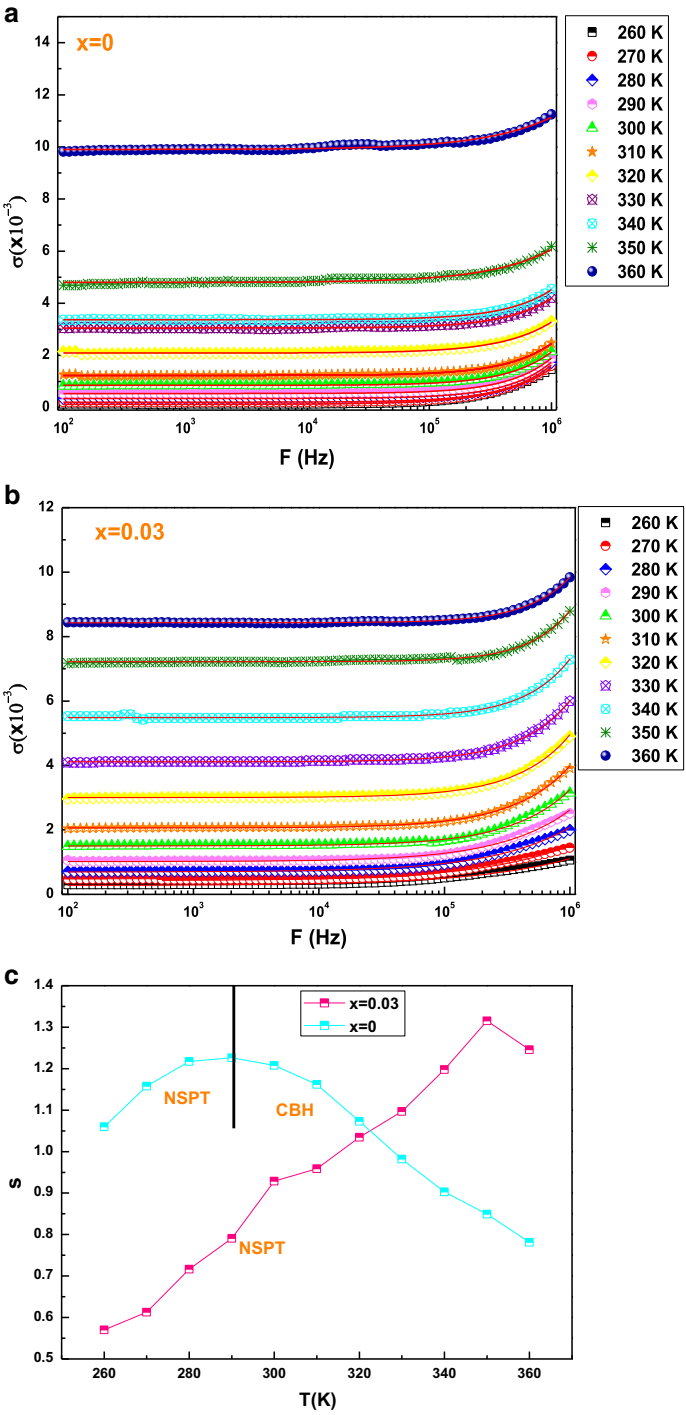

Fig. 8 The variation of the electrical conductivity versus the frequency at different temperatures of: **a** $x = 0$, **b** $x = 0.03$ and **c** the variation of the s exponent for $x = 0.0$ and $x = 0.03$ compounds

On the other hands, the temperature dependence of the (s) exponent for the $x = 0.0$ compound proves the presence of two successful conduction process; NSPT and CBH. While for $x = 0.03$ compound, only NSPT process is observed indicating that the substitution process leads to a homogeneity and uniformity in the conduction process (Fig. 8c). It is also important to mention that at higher temperatures, (s) reaches values higher than unity, which is explained by the species localized jump without leaving the neighborhood [47, 61].

5 Conclusion

To conclude, the XRD examination of the prepared samples proved a $Pm\bar{3}m$ cubic structure with agglomerated nanometric particles, as seen by SEM. The study of the electrical properties in the frequency range of 10^2 Hz–10^6 Hz and temperature range of 260–360 K exhibits an Arrhenius behavior confirmed by the relaxation peak increasing in the Z'' spectra with the increase in temperature. This study of the direct current conductivity for both $x = 0$ and $x = 0.03$ samples proves a VRH process at low temperatures ad an SPH process at higher temperatures. The calculated activation energies show a transformation of the electrical behavior as a function of the substitution process confirmed by a decrease in the resistance of the material. On the other hands, the variation of the AC conductivity presents a Jonscher's behavior with a succession of NSPT and CBH model for $x = 0$ and only CBH one for $x = 0.03$.

Supplementary Information The online version contains supplementary material available at https://doi.org/10.1140/epjp/s13360-021-01780-7.

Acknowledgments The authors acknowledge the support of the Tunisian Ministry of Higher Education and Scientific Research within the framework of the Tunisian-Portuguese cooperation in the field of scientific research and technology (Project of University of Sfax-University of Aveiro). This work was supported by national funds from FCT – Fundação para a Ciência e a Tecnologia, I.P., within the projects UIDB/04564/2020 and UIDP/04564/2020. Access to TAIL-UC facility funded under QREN-Mais Centro Project No. ICT_2009_02_012_1890 is gratefully acknowledged.

References

1. A. Bougoffa, A. Benali, M. Bejar, E. Dhahri, M.P.F. Graca, M.A. Valente, L. Bessais, B.F.O. Costa, J. Alloys Compd. **856**, 157425 (2021)
2. A. Benali, S. Azizi, M. Bejar, E. Dhahri, M.F.P. Graça, J. Ceram. Int. **40**, 14367–14373 (2014)
3. Q. Qi, J. Zhao, R.-F. Xuan, P.-P. Wang, L.-L. Feng, L.-J. Zhou, D.-J. Wang, G.-D. Li, J. Sens. Actuator B Chem. **191**, 659–665 (2014)
4. K.T.C. Roseno, R. Brackmann, M.A. da Silva, M. Schmal, Int. J. Hydrog. Energy **41**, 18178–18192 (2016)
5. S.J. Skinner, Recent advances in perovskite-type materials for SOFC cathodes. J. Fuel Cells Bull. **4**, 6–12 (2001)
6. E. Delgado, C.R. Michel, CO_2 and O_2 sensing behavior of nanostructured barium-doped $SmCoO_3$. J. Mater. Lett. **60**, 1613–1616 (2006)
7. V.S. Kolat, H. Gencer, M. Gunes, S. Atalay, J. Mater. Sci. Eng. B **140**, 212–217 (2007)
8. F.B. Abdallah, A. Benali, M. Triki, E. Dhahri, M.P.F. Graca, M.A. Valente, J. Superlattice Microstruct. **117**, 260–270 (2018)
9. R. Hamdi, A. Tozri, M. Smari, K. Nouri, E. Dhahri, L. Bessais, J. Mol. Struct. **1175**, 844–851 (2019)
10. A. Omri, M. Bejar, E. Dhahri, M. Es-Souni, M.A. Valente, M.P.F. Graça, L.C. Costa, J. Alloys Compd. **536**, 173–178 (2012)
11. Kh. Dhahri, M. Bejar, E. Dhahri, M.J. Soares, M.F.P. Graça, M.A. Sousa, J. Mater. Lett. **128**, 235–237 (2014)

12. Y.D. Kolekar, L.J. Sanchez, C.V. Ramana, J. Appl. Phys. **115**, 144106–144116 (2014)
13. H. Baaziz, A. Tozri, E. Dhahri, E.K. Hlil, J. Chem. Phys. Lett. **691**, 355–359 (2018)
14. R. Ganguly, I.K. Gopalakrishnan, J.V. Yakhmi, J. Phys. B **275**, 308–315 (2000)
15. S. Vadnala, T.D. Rao, P. Pal, S. Asthana, J. Phys. B Condens. Matter **448**, 277–280 (2014)
16. H. Gencer, M. Pektas, Y. Babur, V.S. Kolat, T. Izgi, S. Atalaya, J. Magn. **17**, 176–184 (2012)
17. H. Rahmouni, R. Jemai, N. Kallel, A. Selmi, K. Khirouni, J. Alloys Compd. **497**, 1–5 (2010)
18. S.P. Yadav, S.S. Shinde, A.A. Kadam, K.Y. Rajpure, J. Alloys Compd. **555**, 330 (2013)
19. Z.J. Yue, K. Zhao, H. Ni, S.Q. Zhao, Y.C. Kong, H.K. Wong, A.J. Wang, J. Phys. D Appl. Phys. **44**, 095103–095103 (2011)
20. M. Coskun, F.M. Coskun, Z. Durmus, M. Caglar, A. Turut, Os doped $YMnO_3$ multiferroic: a study investigating the electrical properties through tuning the doping level. J. Alloys Compd. **752**, 274–288 (2018)
21. A. Bougoffa, J. Massoudi, M. Smari, E. Dhahri, K. Khirouni, L. Bessais, J. Mater. Sci. Mater. Electron. **30**, 21018–21031 (2019)
22. I. Pintilie, V. Stancu, A. Tomulescu, R. Radu, C. Besleaga Stan, L. Trinca, L. Pintilie, J. Mater. Des.
23. N. Sivakumar, A. Narayanasamy, C.N. Chinnasamy, B. Jeyadevan, J. Phys. Condens. Mater. **19**, 386201 (2007)
24. Y. Koseoglu, F. Alan, M. Tan, R. Yilgin, M. Ozturk, Ceram. Int. **38**, 3625 (2012)
25. H. Gao, S. Liu, Y. Li, E. Conte, Y. Cao, Energies **10**(11), 1787 (2017)
26. Q. Qi, J. Zhao, R.-F. Xuan, P.-P. Wang, L.-L. Feng, L.-J. Zhou, D.-J. Wang, G.-D. Li, Sens. Actuators B **191**, 659 (2014)
27. K. Fan, H. Qin, L. Wang, L. Ju, J. Hu, Sens. Actuators B **177**, 265 (2013)
28. L. Ma, S.Y. Ma, Z. Qiang, X.L. Xu, Q. Chen, H.M. Yang, H. Chen, Q. Ge, Q.Z. Zeng, B.Q. Wang, Mater. Lett. **200**, 47 (2017)
29. S. Azizi, A. Benali, M. Bejar, E. Dhahri, M.P.F. Graça, M.A. Valente, J. Alloys Compd. **644**, 304 (2015)
30. V.K. Jha, P. Nautiyal, M.M. Seikh, R. Chatterjee, R. Mahendiran, A.K. Kundu, J. Mater. Sci. **48**(21), 7629–7634 (2014). https://doi.org/10.1007/s10853-013-7580-6
31. A.G. Gamzatov, A.M. Aliev, A.B. Batdalov, H. Ahmadvand, H. Sala-mati, P. Kameli, J. Mater. Sci. **49**, 294–299 (2014). https://doi.org/10.1007/s10853-013-7704-z
32. A.J. Millis, Nature **392**, 147–150 (1998)
33. C. Martin, A. Maignan, M. Hervieu, B. Raveau, Phys. Rev. B **60**, 12191–12199 (1999)
34. W. Zhong, C.T. Au, Y.W. Du, Chin. Phys. B **22**, 11–057501 (2013)
35. T. Barbier, C. Autret-Lambert, C. Honstrette, F. Gervais, M. Lethiecq, Mater. Res. Bull. **47**, 4427–4432 (2012)
36. Y.D. Kolekar, L.J. Sanchez, C.V. Ramana, J. Appl. Phys. **115**, 144106 (2014)
37. T.T. Ahmed, I.Z. Rahman, M.A. Rahman, J. Mater. Process. Technol. **797**, 153–154 (2004)
38. N. Dhahri, A. Dhahri, K. Cherif, J. Dhahri, H. Belmabrouk, E. Dhahri, J. Alloys Compd. **507**(2), 405 (2010)
39. E.M. Benali, A. Benali, M. Bejar, E. Dhahri, M.P.F. Graca, M.A. Valente, B.F.O. Costa, J. Mater. Sci. Mater. Electron. **31**, 3197–3214 (2020)
40. H.M. Rietveld, J. Appl. Cryst. **2**, 65 (1965)
41. Y. Koseoglu, F. Alan, M. Tan, R. Yilgin, M. Ozturk, J. Ceram. Int. **38**, 3625–3634 (2012)
42. P. Vousden, Acta Crystallogr. **4**, 545–551 (1951)
43. A. Guinier, IX. Dunod, Théorie et Technique de la radiocristallographie, 3rd edn. (1964), p. 462
44. H. Rahmouni, M. Smari, B. Cherif, E. Dhahri, K. Khirouni, Dalton Trans. **44**, 10457 (2015)
45. S. Brahma, R.N.P. Choudhary, A.K. Thakur, Phys. B **355**, 188 (2005)
46. J.C.C. Abrantes, J.A. Labrincha, J.R. Frade, Mater. Res. Bull. **35**, 727–740 (2000)
47. C. Bharti, T.P. Sinha, J. Phys. B **406**, 1827–1832 (2011)
48. A. Dutta, C. Bharti, T.P. Sinha, J. Phys. B **403**, 3389 (2008)
49. K.S. Cole, R.H. Cole, J. Chem. Phys. **10**, 98–105 (1942)
50. K.P. Padmasree, D.K. Kanchan, A.R. Kulkami, Solid State Ion. **177**, 475 (2006)
51. M. Coskun, O. Polat, F.M. Coskun, Z. Durmus, M. Caglar, A. Turut, J. Mater. Sci. Semicond. Process. **109**, 104923–104935 (2020)
52. F. Elleuch, M. Triki, M. Bekri, E. Dhahri, E.K. Hlil, J. Alloys Compd. **620**, 249–255 (2015)
53. M. Rudra, S. Halder, S. Saha, A. Dutta, T.P. Sinha, J. Mater. Chem. Phys. **230**, 277–286 (2019)
54. N.F. Mott, E.A. Davis, *Electronic Processes in Non-Crystalline Materials* (Clarendon, Oxford, 1979), pp. 1–55
55. H. Rahmouni, B. Cherif, M. Baazaoui, K. Khirouni, J. Alloys Compd. **575**, 5–9 (2013)
56. S. Mollah, H.L. Huang, H.D. Yang, S. Pal, S. Taran, B.K. Chandhuri, J. Magn. Magn. Mater. **284**, 383–394 (2004)

57. W. Hzez, A. Benali, H. Rahmouni, E. Dhari, K. Khirouni, B.F.O. Costa, Effects of oxygen deficiency on the transport and dielectric properties of NdSrNbO. J. Phys. Chem. Solids **117**, 1–12 (2018)
58. E. Barsoukov, J. Ross Macdonald, *Impedance Spectroscopy Theory, Experiment and Applications*, 2nd edn. (Wiley, New York, 2005), p. 14
59. A.K. Jonscher, *Universal Relaxation Law* (Chelsea Dielectric Press, London, 1996)
60. C. Bharti, T.P. Sinha, J. Phys. B Condens. Mater. **406**, 1827–1832 (2011)
61. K. Funke, Jump relaxation in solid electrolytes. Prog. J. Solid State Chem. **22**, 111–195 (1993)